Ground-state magnetic structures of topological kagome metals $R\mathrm{V_6Sn_6}$ (R = Tb, Dy, Ho, Er)

Yishui Zhou [1,2] Min-Kai Lee [3] Sabreen Hammouda [1] Sheetal Devi [1] Shin-Ichiro Yano [4] Romain Sibille,[5]
Oksana Zaharko [5] Wolfgang Schmidt [6] Karin Schmalzl [6] Ketty Beauvois,[7] Eric Ressouche [7] Po-Chun Chang [1,8]
Chun-Hao Huang,[1] Lieh-Jeng Chang [3,*] Thomas Brückel [9] and Yixi Su [1,†]

[1]*Jülich Centre for Neutron Science (JCNS) at the Heinz Maier-Leibnitz Zentrum (MLZ), Forschungszentrum Jülich,
Lichtenbergstrasse 1, D-85747 Garching, Germany*

[2]*Technical University of Munich (TUM), TUM School of Natural Sciences, Physics Department, D-85747 Garching, Germany*

[3]*Department of Physics, National Cheng Kung University (NCKU), Tainan 70101, Taiwan*

[4]*National Synchrotron Radiation Research Center, Hsinchu 30077, Taiwan*

[5]*Laboratory for Neutron Scattering and Imaging, PSI Center for Neutron and Muon Sciences, Forschungsstrasse 111,
5232 Villigen, PSI, Switzerland*

[6]*Jülich Centre for Neutron Science (JCNS) at ILL, Forschungszentrum Jülich, F-38000 Grenoble, France*

[7]*Université Grenoble Alpes, CEA, IRIG, MEM, MDN, F-38000 Grenoble, France*

[8]*Department of Physics, Tamkang University, Tamsui 251301, Taiwan*

[9]*Jülich Centre for Neutron Science JCNS and Peter Grünberg Institut PGI, JARA-FIT, Forschungszentrum Jülich, D-52425 Jülich, Germany*

Magnetic kagome metals have attracted tremendous research interests recently, because they represent an ideal playground for exploring the fascinating interplay between their intrinsically inherited topologically nontrivial electron band structures, magnetism and electronic correlation effects, and the resultant novel electronic/magnetic states and emergent excitations. In this work, we report a comprehensive single-crystal neutron diffraction investigation of the ground-state magnetic structures of the recently discovered V-based topological kagome metals $R\mathrm{V_6Sn_6}$ (R = Tb, Dy, Ho, Er). Furthermore, the sample synthesis details and our systematic studies of crystal structure, low-temperature magnetic and thermodynamic properties of these compounds via various in-house characterization techniques are also reported. Our single-crystal neutron diffraction measurements confirm that the long-range magnetic order forms below 4.3 K for R = Tb, 3.0 K for R = Dy, 2.4 K for R = Ho, and 0.6 K for R = Er, respectively. The ground-state magnetic structures of the studied compounds are comprehensively determined via the magnetic crystallography approaches. It can be revealed that $R\mathrm{V_6Sn_6}$ (R = Tb, Dy, Ho) have a collinear ferromagnetic order in the ground state, with the ordered magnetic moment aligned along the c axis for R = Tb, Ho, while approximately $20°$ tilted off from the c axis for R = Dy. In contrast, $\mathrm{ErV_6Sn_6}$ shows an A-type antiferromagnetic structure with a magnetic propagation vector $\mathbf{k} = (0, 0, 0.5)$, and with the ordered magnetic moment aligned in the ab plane. The ordered magnetic moments are determined as 9.4(2) μ_B, 6.6(2) μ_B, 6.4(2) μ_B, and 6.1(2) μ_B for R = Tb, Dy, Ho, and Er, respectively. A comparison of the low-temperature magnetic structures for both the extensively investigated topological kagome metal series of $R\mathrm{V_6Sn_6}$ and $R\mathrm{Mn_6Sn_6}$ is given in detail. This allows to gain new insights into the complex magnetic interactions, diverse single-ion magnetic anisotropies and spin dynamics in these compounds. The reported ground-state magnetic structures in $R\mathrm{V_6Sn_6}$ (R = Tb, Dy, Ho, Er) can pave the way for further explorations of the possible interplay between magnetism and topologically nontrivial electron band structures in the magnetically ordered phase regime.

I. INTRODUCTION

Topological metals and semimetals possessing a two-dimensional kagome lattice are an ideal platform for the studies of quantum interactions between geometric effects of lattice, topologically nontrivial electron band structures, magnetism, and electronic correlations, owing to some extraordinary features in their electronic structures such as Dirac cones, flat bands, and van Hove singularities [1–4]. For instance, Dirac cones are a defining feature in electronic structure that can lead to topologically protected states, flat bands can be a fertile ground for unconventional superconductivity, and van Hove singularities can lead to instabilities towards exotic electronic orders [5–7]. Emergent correlated topological phases are widely found in kagome metals and semimetals, such as magnetic Weyl fermions in $\mathrm{Mn_3Sn}$ [8–12] and $\mathrm{Co_3Sn_2S_2}$ [13–17], massive Dirac fermions in

---

Fe$_3$Sn$_2$ [18–22], quantum-limited magnetic Chern phases in TbMn$_6$Sn$_6$ [23–26], charge-density waves (CDW) in FeGe [27] and ScV$_6$Sn$_6$ [28–36], and both CDW and superconductivity in AV$_3$Sb$_5$ (A = K, Rb, Cs) [37–41].

Among them, the intermetallic RT$_6$Sn$_6$ (R = rare earths, T = transition metals) compound stands out for its unique crystal structure of HfFe$_6$Ge$_6$-type (space group No. 191, P6/mmm), that has a kagome bilayer structure formed by transition metal element and in-between a triangular layer of rare-earth element stacked along the c axis in the unit cell. Recently, the RMn$_6$Sn$_6$ series has attracted a lot of attention not only for its complex magnetism due to rich magnetic interactions from the Mn-Mn, R-Mn, and R-R couplings, but also for the intrinsic tunability of the magnetic properties by rare-earth elements that have distinct single-ion magnetic anisotropies [7,23,26,42–56]. The RMn$_6$Sn$_6$ (R = Gd, Tb, Dy, and Ho) compounds are all ferrimagnetic (FiM) but with different magnetic anisotropy, for instance, in-plane for R = Gd, out-of-plane for R = Tb, tilted off from the c axis for R = Dy, Ho, while other RMn$_6$Sn$_6$ compounds (R = Sc, Y, Er, Tm, and Lu) have an incommensurate helical magnetic order over a large temperature range. Such a high diversity in magnetic anisotropy and magnetic structure allows the rare-earth engineering of various topological quantum phases [52].

Similarly, the kagome metal RV$_6$Sn$_6$ series was recently discovered and has also attracted strong interests due to rich quantum phenomena and high diversity in magnetic properties, in which nonmagnetic V replaces Mn in the kagome layers, and the magnetic interaction is mainly contributed by the intralayer and interlayer R-R couplings. For the nonmagnetic RV$_6$Sn$_6$ (R = Sc, Y, Lu) compounds, the CDW was found in ScV$_6$Sn$_6$ at 92 K [28] and thus it has attracted much attention [29–36], the electronic properties of the nonmagnetic YV$_6$Sn$_6$ exhibit high mobility and multiband transport [57,58], but there is not so much study on LuV$_6$Sn$_6$ besides specific heat capacity [58]. For the magnetic RV$_6$Sn$_6$ (R = Gd, Tb, Dy, Ho, Er, Tm) compounds, the magnetic transition temperatures are 4.9 K, 4.2 K, 3.0 K, and 2.4 K for R = Tb, Dy, and Ho, respectively, but no magnetic order observed for R = Er and Tm down to 1.8 K [58,59]. Recent angle-resolved photon-emission spectroscopy (ARPES) studies of GdV$_6$Sn$_6$ and HoV$_6$Sn$_6$ found indeed Dirac cones, saddle points, and flat bands in electronic structure [60], and proved the presence of the topologically nontrivial states in GdV$_6$Sn$_6$ [61]. Furthermore, a finite spin Berry curvature in RV$_6$Sn$_6$ (R = Tb, Ho, Sc) has been unveiled [30]. Besides, an incommensurate magnetic order with the magnetic moments oriented in the ab plane was found in GdV$_6$Sn$_6$ via resonant x-ray diffraction [62], while the magnetism in TbV$_6$Sn$_6$ was found highly anisotropic with easy axis along the c axis [63,64]. In addition, partial crystallographic disorder and a large easy-plane magnetic anisotropy were found in SmV$_6$Sn$_6$ [65], and YbV$_6$Sn$_6$ was discovered as a heavy-fermion compound hosting a triangular Kondo lattice [66]. A study of the magnetic and magnetotransport properties on DyV$_6$Sn$_6$ and HoV$_6$Sn$_6$ found that they have ferromagnetic interaction along the c axis and antiferromagnetic interaction within the ab plane and are multiband systems [67]. Despite extensive recent investigations on the magnetic properties of the kagome metals RV$_6$Sn$_6$

(R = Tb, Dy, Ho, Er) [58,59,63,64,67], their ground-state magnetic structures, which are essential for the understanding of the intertwined topological and magnetic properties in these compounds, have not been determined so far.

In this work, we report a comprehensive single-crystal neutron diffraction study of the low-temperature magnetic properties of the recently discovered V-based topological kagome metals of RV$_6$Sn$_6$ (R = Tb, Dy, Ho, Er). Our single-crystal neutron diffraction measurements confirm the occurrence of the long-range magnetic order at 4.3 K for R = Tb, 3.0 K for R = Dy, 2.4 K for R = Ho, and 0.6 K for R = Er, respectively. Based on the magnetic crystallography approaches, the ground-state magnetic structures of the studied compounds are comprehensively determined. The RV$_6$Sn$_6$ (R = Tb, Dy, Ho) compounds have a collinear ferromagnetic order below the respective magnetic phase transition temperature, with the ordered magnetic moment aligned along the c axis for R = Tb, Ho, while approximately $20°$ tilted off from the c axis for R = Dy. ErV$_6$Sn$_6$ shows an A-type antiferromagnetic structure with a magnetic propagation vector $\mathbf{k}$ = (0, 0, 0.5), and with the ordered moment aligned in the ab plane. The ordered magnetic moments are determined as 9.4(2) μ_B, 6.6(2) μ_B, 6.4(2) μ_B, and 6.1(2) μ_B for R = Tb, Dy, Ho, and Er, respectively. In addition, we also report the sample synthesis via the flux-method crystal growth, and the systematic investigations of crystal structures, magnetic properties and specific heat capacity (down to 50 mK) of the high-quality single-crystal samples of this kagome metal series via a wide range of in-house characterization techniques. A comparison of the low-temperature magnetic structures in both RV$_6$Sn$_6$ and RMn$_6$Sn$_6$ kagome metal series is given. This allows to shed light on the complex magnetic interactions, diverse single-ion magnetic anisotropies and spin dynamics in these compounds. Our study would motivate further investigations on the possible interplay between magnetism and topologically non-trivial electron band structures in the magnetically ordered phase regime in this fascinating topological kagome metal series of RV$_6$Sn$_6$.

II. EXPERIMENTAL DETAILS

Single crystals of RV$_6$Sn$_6$ were grown via the self-flux method. Rare-earth element pieces, V granular, and Sn shots were loaded in a crucible in the glove box with the molar ratio of R : V : Sn = 1 : 2 : 40, which was then sealed in a quartz tube under an argon atmosphere with the pressure of 200 mbar. The tube was heated to 1200°C over 12 hours and then dwelt for 10 hours. Afterwards, it was slowly cooled down to 800°C with a cooling rate of 1°C/h followed by centrifuging to separate crystals from the flux, and then shiny plate-shape crystals were obtained (see Fig. 1).

In-house single-crystal x-ray diffraction (XRD) was measured using a Rigaku XtaLAB Synergy-S diffractometer with MoK$_\alpha$. The CrysAlis^{Pro} software is used to search for a proper unit cell, and after indexing, to integrate the intensity of the Bragg reflections over different image frames. The absorption correction is done using the indexed crystal facets. The Jana2006 program is used for the crystal structure refinement and the charge flipping approach for solving crystal structures [68].
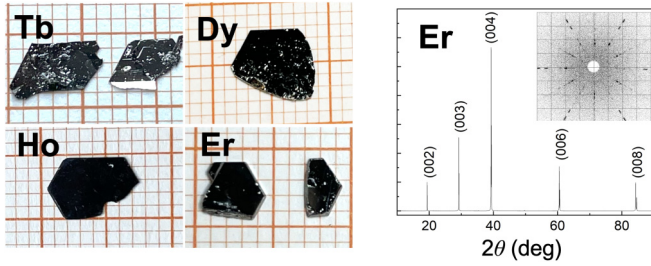
FIG. 1. Single crystals of RV$_6$Sn$_6$ (R = Tb, Dy, Ho, Er) via self-flux method and x-ray diffraction pattern of ErV$_6$Sn$_6$ single crystal in the c direction, the inset shows the Laue x-ray pattern in the same direction.

A few selected single crystals were used for measuring the magnetic properties by SQUID from Quantum Design. Magnetic susceptibility ($M/H - T$) was measured with sweeping temperature from 300 to 2 K under a magnetic field of 1 T. The isothermal magnetization ($M - H$) curves were measured from 0 to 5 T at different temperatures.

The molar heat capacity at constant pressure (C_p) of the RV$_6$Sn$_6$ single crystals was measured using a PPMS device from Quantum Design. After the addenda measurement, the samples with suitable mass and size were chosen to optimize the thermal coupling between the sample and the puck. Specific heat was measured in two temperature ranges, from 50 mK to 3 K and from 2 K to 100 K, and then the data were combined accordingly. Note that only the low-temperature part for DyV$_6$Sn$_6$ and only the high-temperature part for LuV$_6$Sn$_6$ were measured.

Comprehensive single-crystal neutron diffraction experiments were carried out with a series of neutron instruments at various neutron facilities. For TbV$_6$Sn$_6$, a 3 mg high-quality single crystal was chosen and mounted on an aluminium pin with GE-vanish. The neutron diffraction experiment was conducted at the thermal neutron single-crystal diffractometer Zebra at SINQ, PSI. A neutron beam with wavelength of 1.383 Å was generated using a Ge(311) monochromator. An open HUBER cradle combined with a dedicated 1.6-300 K cryostat (JT-CCR) was used. Initially, an area detector was utilized to locate the peaks and subsequently switched to a single detector configuration for data collection. Neutron diffraction measurements on the HoV$_6$Sn$_6$ and ErV$_6$Sn$_6$ single crystals were initially performed using the cold neutron triple-axis spectrometer (TAS) Sika at ANSTO. The samples, weighing 33.2 mg and 42.6 mg, respectively, were mounted in the (H, H, L) horizontal scattering plane. All elastic scans were performed with $\mathbf{k}_i = \mathbf{k}_f = 2.662$ Å^{-1}. A PG filter and collimators with a sequence of $0' - 0' - 60' - 60'$ were employed in the experiment. A dilution refrigerator (DF-1) was used for reaching the base temperature of 50 mK for ErV$_6$Sn$_6$. Due to the limited reflections accessible with a cold TAS instrument, while the magnetic propagation vector and the phase transition temperature for both compounds were determined, their magnetic structures could not be solved based on a small number of reflections in the horizontal scattering plane. Further single-crystal neutron diffraction experiments on DyV$_6$Sn$_6$, HoV$_6$Sn$_6$, and ErV$_6$Sn$_6$, with a sample weight at 36.1, 40.9, and 30.7 mg, respectively, were carried out
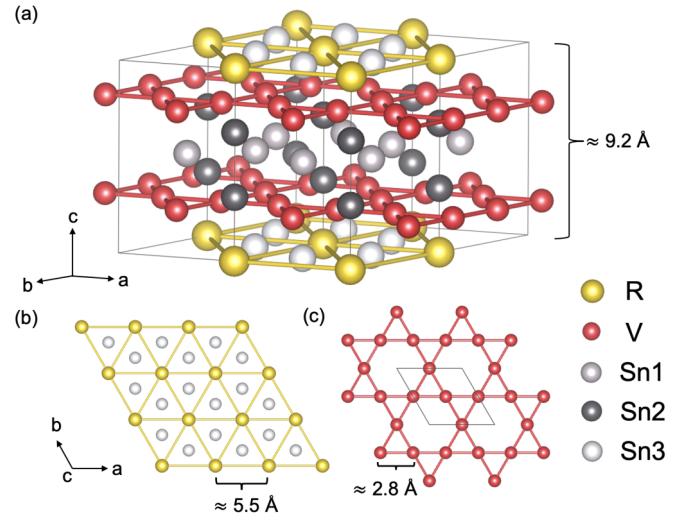

FIG. 2. Crystal structure of RV$_6$Sn$_6$. (a) Hexagonal structure formed by RSn, V, and Sn layers, with the order of [-RSn2-V-Sn3-Sn1-Sn3-V-], and the distance between two adjacent R layers is about 9.2 Å. (b) Triangular structure of R sublattice from the top view, with Sn2 in the middle of each triangular, and the distance between the nearest R ions in the same layer is about 5.5 Å. (c) Kagome structure of V sublattice from the top view, the distance between the nearest V ions is about 2.8 Å.

on the thermal neutron diffractometer D23 at ILL. All measured single-crystal samples at D23 were also mounted in the (H, H, L) horizontal scattering plane, nevertheless, the lifting-counter setup at D23 allows the measurement of out-of-plane reflections. A wavelength of 1.283 Å was employed for data collection. A standard ILL 1.5-300 K orange cryostat combined with a dilution insert was used for ErV$_6$Sn$_6$. All neutron diffraction experiments were carried out under zero magnetic field, and the refinement of magnetic structure as well as neutron absorption correction have been done with the help of Mag2Pol [69]. The momentum transfer $\mathbf{Q} = (H, K, L)$ is defined in hexagonal reciprocal lattice units (r.l.u.) based on the lattice constants given in Tables I and II, where H, K, and L are Miller indices. Both $\mathbf{Q}$ and sample-rotation (i.e., Omega) scans were measured for various reflections.

III. IN-HOUSE CHARACTERIZATION RESULTS

A. X-Ray Diffraction and Crystalline Structures

The crystal structure of RV$_6$Sn$_6$ (R = Tb, Dy, Ho, Er, Lu) is determined through the refinement of single-crystal XRD data collected at room temperature. As depicted in Fig. 2(a), all compounds exhibit a HfFe$_6$Ge$_6$-type hexagonal structure with the space group $P6/mmm$ (No. 191). In this structure, R(1a) and V(6i) ions occupy a single Wyckoff position, while Sn ions are found in three distinct Wyckoff positions, namely, Sn1(2d), Sn2(2e), and Sn3(2c). Along the c axis, the layers are arranged in the sequence of [-RSn3-V-Sn2-Sn1-Sn2-V-]. R ions form a triangular layer with Sn3 situated at the center of each triangle [see Fig. 2(b)], with an approximate interionic distance of 5.5 Å between the nearest R ions. Within a single layer, V ions adopt a perfect kagome structure [see Fig. 2(c)], with the nearest V-V distance at around 2.8 Å. The unit cell

TABLE I. Crystal parameters and physical properties of RV_6Sn_6 ($R =$ Tb $-$ Er, Lu). a, c, and V are refined crystal parameters of RV_6Sn_6 of x-ray single crystal diffraction at room temperature. θ_{CW}^{ab} and θ_{CW}^{c} are the fitted Curie temperatures obtained from the Curie-Weiss fitting on susceptibility with the magnetic field applied within the ab plane and along the c axis. μ_{eff}^{ab} and μ_{eff}^{c} are the fitted effective magnetic moments for R^{3+} ion according to the Curie constant, and the $\mu_{eff}^{free}(\mu_B)$ is the effective moment of free R^{3+} ion. R_{ani} represents the anisotropy ratio, obtained from the susceptibility in the easy-axis direction over in the hard-axis direction at 2 K under the magnetic field of 5 T. $T_{C/N}(K)$ is the transition temperature obtained by heat capacity measurements under zero field (Note that the T_C value of TbV_6Sn_6 is taken from the DC magnetization measurement).

Parameter	TbV_6Sn_6	DyV_6Sn_6	HoV_6Sn_6	ErV_6Sn_6	LuV_6Sn_6
a(Å)	5.5214(2)	5.5161(2)	5.5157(4)	5.5113(2)	5.4976(2)
c(Å)	9.1791(2)	9.1872(6)	9.1774(2)	9.1752(2)	9.1846(2)
V(Å³)	242.34(1)	242.09(1)	241.80(1)	241.35(1)	240.40(1)
$\theta_{CW}^{ab}(K)$	−49.29	−11.88	−5.21	0.76	–
$\theta_{CW}^{c}(K)$	33.92	6.48	9.29	−25.08	–
$\mu_{eff}^{ab}(\mu_B)$	10.28	11.19	10.41	9.41	–
$\mu_{eff}^{c}(\mu_B)$	9.29	11.09	10.41	9.42	–
$\mu_{eff}^{free}(\mu_B)$	9.72	10.65	10.61	9.58	–
Easy axis/plane	c-axis	c-axis	c-axis	ab-plane	–
R_{ani}	181	1.2	10	23	–
$T_{C/N}(K)$	4.0	2.9	2.3	0.5	–

contains two V kagome layers, and the distance between adjacent R layers, also referred to as the c lattice parameter, is approximately 9.2 Å. Further details regarding the lattice parameters can be found in Table I.

B. DC Magnetization

The results from the direct current (DC) magnetization measurements of RV_6Sn_6 (R = Tb, Dy, Ho, Er) single crystals are shown in Fig. 3, with each compound measured with the magnetic field applied within the ab plane and along the c axis. Figures 3(a)–3(d) show the susceptibilities under the

magnetic field of 1 T and measured during cooling from 300 K to 2 K. These results demonstrate that the compounds display strong magnetic anisotropy. Specifically, TbV_6Sn_6 and HoV_6Sn_6 exhibit an easy axis along the c-axis direction, while ErV_6Sn_6 exhibits an easy direction within the ab plane. In comparison, the anisotropy in DyV_6Sn_6 is relatively weak, with the susceptibility along the c direction slightly larger than within the ab plane. The insets in Figs. 3(a)–3d present reciprocal susceptibilities and Curie-Weiss fittings (indicated by blue lines) for each compound. Curie-Weiss fittings were performed in the temperature range of $150 - 300$ K, using the formula $\chi(T) = \chi_0 + C/(T - \theta_{CW})$. The values of
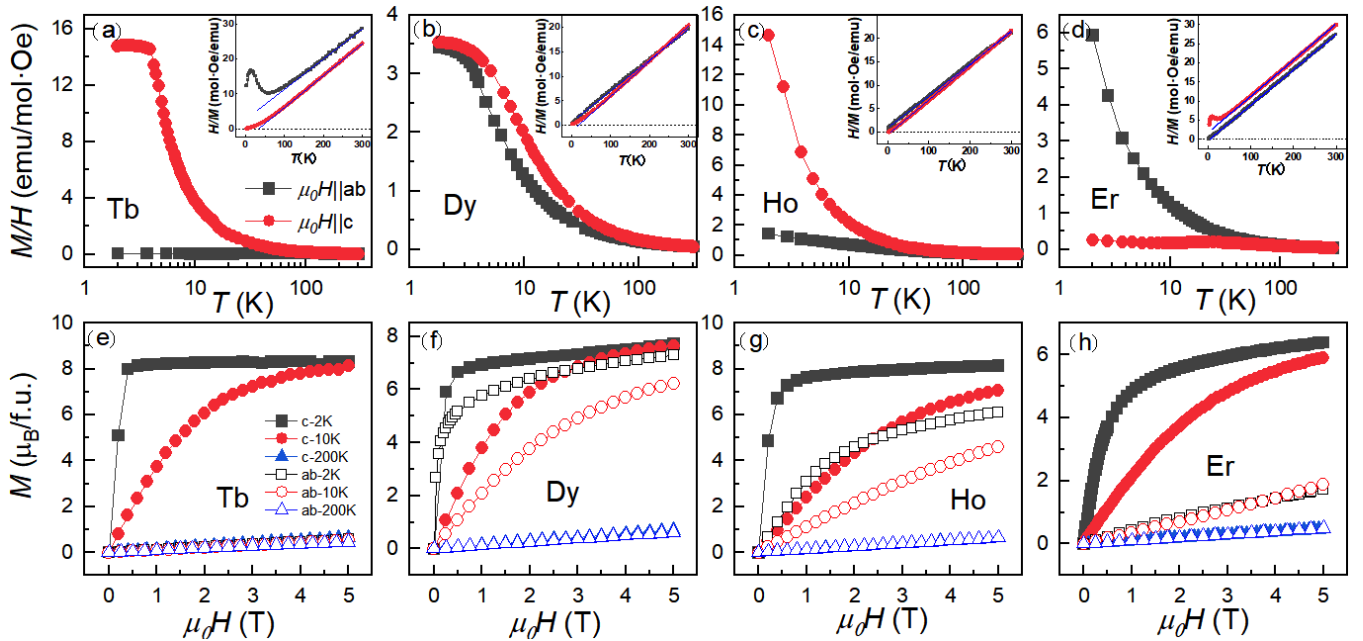

FIG. 3. Magnetic properties of RV_6Sn_6 (R = Tb, Dy, Ho, Er), measured with the magnetic field applied within the ab plane ($\mu_0H||ab$) and along the c axis ($\mu_0H||c$). (a)−(d) sho ws the susceptibilities under the magnetic field of 1 T measured during cooling, and the insets are the reciprocal of susceptibilities and Curie-Weiss fitting. (e)−(h) shows the corresponding isothermal magnetization properties at different temperatures.
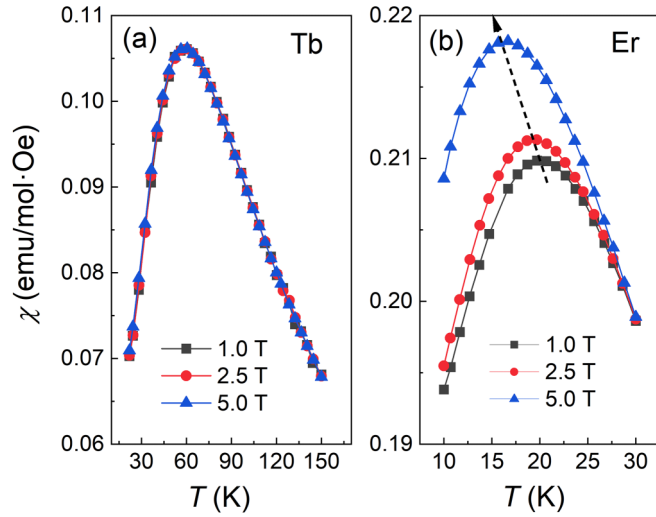
FIG. 4. Broad peaks of susceptibility properties under different magnetic fields applied perpendicular to the easy-axis direction for (a) TbV_6Sn_6 and (b) ErV_6Sn_6.

FIG. 5. Heat capacity of RV_6Sn_6 (R = Tb, Dy, Ho, Er) compounds measured at zero magnetic field down to 50 mK.

the χ_0 for these fittings are in the range of $10^{-4} - 10^{-3}$ emu/mol Oe. The resulting Curie-Weiss temperatures for both in-plane (θ_{CW}^{ab}) and out-of-plane (θ_{CW}^c) directions are shown in Table I. The negative θ_{CW}^{ab} and positive θ_{CW}^c for R = Tb, Dy, and Ho imply antiferromagnetic (AFM) interaction within the ab plane and ferromagnetic (FM) interaction along the c axis, while the situation for ErV_6Sn_6 is to the contrary. The calculated effective magnetic moments, derived from the Curie-Weiss fitting, are also listed in Table I as $\mu_{\text{eff}}^{ab}/\mu_{\text{eff}}^c$, with values of $10.28/9.29\,\mu_B$, $11.19/11.09\,\mu_B$, $10.41/10.41\,\mu_B$, and $9.41/9.42\,\mu_B$ for Tb, Dy, Ho, and Er compounds, respectively. These values closely resemble those of the free R^{3+} ions, indicating that the trivalent valence of rare earth elements and the nonmagnetic nature of V ions. Our susceptibility properties and the Curie-Weiss fitting results are consistent with the previous studies [58,59,67].

Figures 3(e)–3(h) present the magnetization of these compounds at different temperatures, in which the anisotropy shows evidently, particularly at low temperatures. To assess the level of anisotropy, an anisotropic ratio R_{ani} was defined as the ratio of magnetization in the easy direction to that in the hard direction at 2 K and under a 5 T magnetic field where the spin moments are more or less saturated. The values of R_{ani} for these compounds are listed in Table I. TbV_6Sn_6 exhibiting extreme anisotropy along the c axis, characterized by an R_{ani} value of 181, suggests an Ising transition at low temperature which is consistent with former studies [63,64], while a very weak anisotropy along the c axis of R_{ani} value 1.2 for DyV_6Sn_6. The anisotropy for HoV_6Sn_6 is also along the c axis and stronger than DyV_6Sn_6 but smaller than TbV_6Sn_6, with the anisotropy ratio of 10. ErV_6Sn_6 displays an easy direction within the ab plane, and a relatively strong anisotropy with the R_{ani} values of 23.

In addition, a broad feature is observed in the susceptibilities of TbV_6Sn_6 and ErV_6Sn_6 compounds, as shown in Fig. 4, specifically along the direction perpendicular to the easy axis. Under different magnetic fields, the susceptibilities of TbV_6Sn_6 [see Fig. 4(a)] compounds remain unchanged
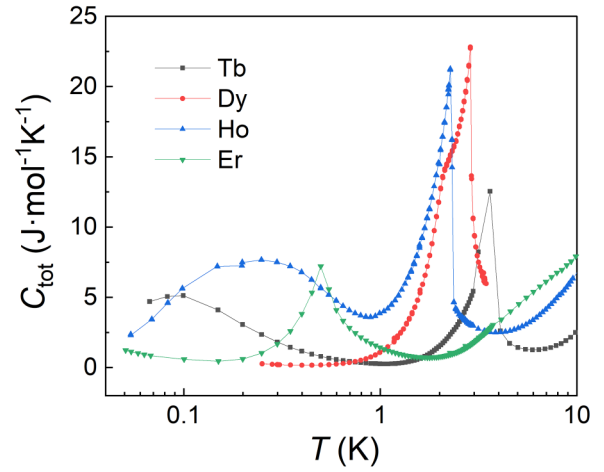
up to 5 T. However, in the case of ErV_6Sn_6 [see Fig. 4(b)] compound, the broad peak shifts slightly to lower temperatures and exhibits higher susceptibility when a larger magnetic field is applied. A similar behavior was also observed in TbV_6Sn_6 by Pokharel *et al.* [64]. This broad-peak feature is likely due to the gradual development of single-ion magnetic anisotropy at low temperatures.

C. Heat Capacity

Figure 5 shows the temperature dependence of the specific heat for the compounds RV_6Sn_6 (R = Tb, Dy, Ho, and Er) down to 50 mK. In agreement with the magnetization studies, a λ-shape sharp heat capacity anomaly is observed at low temperatures for all the compounds, providing further support for the presence of long-range magnetic order at their ground states. The transition temperatures for Tb, Dy, Ho, and Er compounds are identified at $\sim$3.6 K, 2.9 K, 2.3 K, and 0.5 K, respectively. Our results are consistent with the recent studies on this series [58,59], but it should be noted that the previous results are limited to 1.8 K. Besides, there is only one sharp peak for each compound down to 50 mK, and the additional broad or upturn feature below the long-range magnetic ordering temperature can be observed at very low temperatures in TbV_6Sn_6, HoV_6Sn_6, and ErV_6Sn_6, which is attributed to the nuclear Schottky heat-capacity contribution from the respective R^{3+} ions. The nuclear Schottky anomaly is resulted from the splitting of the energy levels due to the hyperfine interaction between the electronic and nuclear spins of the R^{3+} ions. Such hyperfine interactions can be rather large in some rare-earth elements such as Ho and Tb, thus leading to prominent nuclear Schottky anomaly that has widely been observed in various rare-earth based magnetic materials [70–73]. A detailed analysis of the low-temperature heat capacity data of the studied compounds will be discussed in a separate work of ours together with nonmagnetic LuV_6Sn_6.

IV. MAGNETIC STRUCTURE DETERMINATION VIA SINGLE-CRYSTAL NEUTRON DIFFRACTION

Having evidenced the presence of long-range magnetic order in their respective ground states, we turn to single-crystal

TABLE II. Single-crystal neutron diffraction results for RV_6Sn_6 (R = Tb, Dy, Ho, Er). $T_{C/N}(K)$ is the magnetic transition temperature obtained from the temperature dependent neutron diffraction measurements under zero field. The lattice parameters a and c are obtained based on the single-crystal neutron diffraction data taken below $T_{C/N}$ at the base temperature of 1.6 K, 1.8 K, 1.8 K, and 50 mK for R = Tb, Dy, Ho, and Er, respectively. V($6i$) and Sn2($2e$) represent the refinable Wyckoff positions for the crystal structure with space group $P6$/mmm. The refinements of the atomic positions of V($6i$) and Sn2($2e$) are performed based on the single-crystal neutron diffraction data taken both at HT (i.e., at 5.5, 5.0, 5.0, and 0.7 K for Tb, Dy, Ho, and Er compounds, respectively), and at LT (i.e., at 1.6, 1.8, 1.8, and 0.05 K for Tb, Dy, Ho, and Er compounds, respectively). **k** is the magnetic propagation vector. $\mathbf{M}_{[1,0,0]}$, $\mathbf{M}_{[1,2,0]}$, and $\mathbf{M}_{[0,0,1]}$ are the projection of the magnetic moment along [1, 0, 0], [1, 2, 0], and [0, 0, 1] determined by the refinement, and the $\mu_{\mathrm{eff}}^{\mathrm{free}}(\mu_B)$ is the effective moment of free R^{3+} ion. The refinement parameter $R_F(Int)$ represents the average discrepancy between the observed and calculated values of the integrated intensity of the reflections, serving as a measure of the agreement between the experimental data and the theoretical model.

Parameter	TbV_6Sn_6	DyV_6Sn_6	HoV_6Sn_6	ErV_6Sn_6
$T_{C/N}(K)$	4.3	3.0	2.4	0.6
a(Å)	5.530(9)	5.510(7)	5.506(6)	5.50(1)
c(Å)	9.212(6)	9.167(6)	9.158(9)	9.181(8)
V($6i$) (HT)	0.2562(4)	0.2460(9)	0.2553(9)	0.2655(7)
V($6i$) (LT)	0.2488(4)	0.2496(9)	0.2517(7)	0.2665(4)
Sn2($2e$) (HT)	0.3343(5)	0.3339(5)	0.3311(5)	0.3321(8)
Sn2($2e$) (LT)	0.3346(5)	0.3338(6)	0.3298(6)	0.3315(8)
k	(0, 0, 0)	(0, 0, 0)	(0, 0, 0)	(0, 0, 0.5)
$\lvert\mathbf{M}_{[1,0,0]}\rvert(\mu_B)$	0	2.3(2)	0	6.1(3)
$\lvert\mathbf{M}_{[1,2,0]}\rvert(\mu_B)$	0	0	0	0
$\lvert\mathbf{M}_{[0,0,1]}\rvert(\mu_B)$	9.4(2)	6.2(1)	6.4(2)	0
$\mu_{\mathrm{eff}}^{\mathrm{free}}(\mu_B)$	9.72	10.65	10.61	9.58
$R_F(Int)$	1.96	5.53	3.84	3.09

neutron diffraction, a microscopic probe, to determine the magnetic structures of these four compounds. The first step is to identify the magnetic propagation vector of the ordered magnetic moment below its transition temperature. When the reflections with both structural and magnetic information are measured, there are several approaches to solve magnetic structure via refinement. If the magnetic propagation vector is commensurate, one can solve the magnetic structure employing the irreducible representations (Irreps) or magnetic space group (MSG). When the propagation vector is incommensurate, the approach using magnetic super-space group (MSSG) needs to be introduced.

In this work, all the studied RV_6Sn_6 (R = Tb, Dy, Ho, Er) compounds have a commensurate propagation vector, the Irreps are calculated with the space group P6/mmm by SARAh [74] to obtain the allowed basis vectors. One difficulty in this series is that the V is almost invisible because of its rather small nuclear coherent scattering length for neutrons, so the atomic positions of both V($6i$) and Sn2($2e$) that are obtained from the structural refinement based on the XRD data taken at room temperature are used as the initial input parameters for the refinement of the neutron diffraction data. The refinements of the atomic positions of V($6i$) and Sn2($2e$) are performed based on the single-crystal neutron diffraction data taken at HT (i.e., slightly above $T_{C/N}$), and at LT (i.e., below $T_{C/N}$ at the base temperatures). No appreciable changes of the atomic positions of both V($6i$) and Sn2($2e$) can be seen (see Table II). Furthermore, the Omega scans, that are carefully performed for all samples at both HT and LT, do not show any changes in their peak position and peak width (see the following subsections). Therefore, we conclude that a concomitant structure phase transition at $T_{C/N}$ is unlikely, at least, within the detection limits of our neutron diffraction

experiments. Since the absorption cross-sections of Dy and Er are about 994 and 159 barn for thermal neutrons, respectively, which is notably high when compared to other rare-rare elements, thus neutron absorption correction is needed. One can deal with the absorption correction via Mag2Pol [69,75], in which a 3-dimensional crystal model can be created based on the shape and size of the real sample on which the neutron diffraction is performed, then the intensity of the measured reflections can be corrected according to the distance that the neutron beam travels inside the sample. All the single-crystal diffraction results for RV_6Sn_6 (R = Tb, Dy, Ho, Er) are listed in Table II. It is worth noting that the lattice parameters of TbV_6Sn_6 at 1.6 K obtained via neutron diffraction (see Table II) are slightly larger than that obtained at room temperature via XRD (see Table I). This is rather unusual and potentially interesting, further experiments, such as low-temperature XRD measurements, or low-temperature strain measurements on single-crystal samples using strain gauges and capacitance bridges, would be very helpful to clarify this.

A. Magnetic Structure of TbV_6Sn_6

The single-crystal neutron diffraction results of TbV_6Sn_6 are shown in Fig. 6. As shown in Fig. 6(a), it can be seen that the magnetic phase transition takes place at 4.3 K. The (1, 0, -1) reflection is chosen to do the temperature dependent measurement for the reason that the contribution from structural intensity here is almost zero and the change in magnetic intensity can be seen clearly [see Fig. 6(d)]. The intensity of the (0, 0, 2) reflection shows no difference between 5.5 K and 1.6 K, indicating that the magnetic moment is strictly aligned along the c axis, which is consistent with the magnetization results (see Fig. 3). A ferromagnetic order
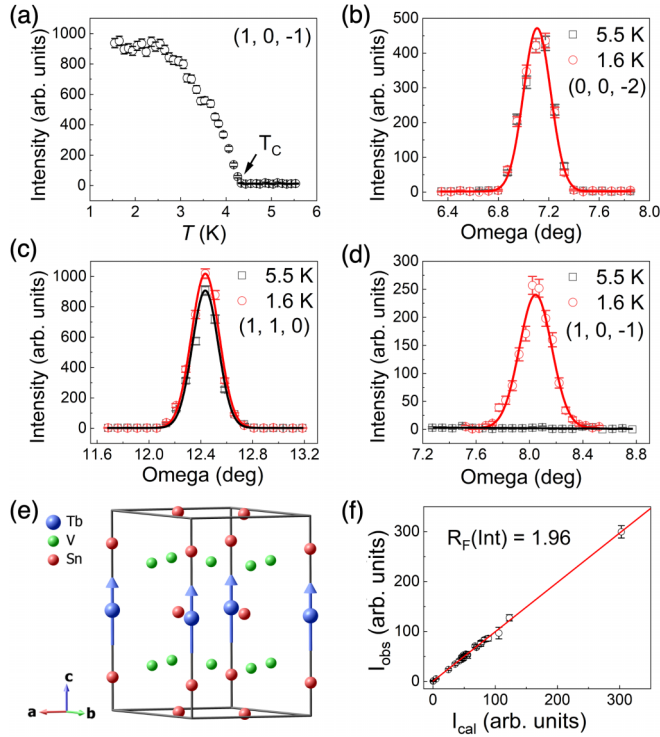
FIG. 6. Single-crystal neutron diffraction results of TbV$_6$Sn$_6$. (a) Temperature dependence from 1.6 K to 5.5 K of (1, 0, -1). (b)–(d) Omega scans at 5.5 K and 1.6 K of (0, 0, -2), (1, 1, 0), and (1, 0, -1). (e) Magnetic structure of TbV$_6$Sn$_6$ with the magnetic propagation vector **k** = (0, 0, 0), and (f) fitted reflections as a function of observation and calculation.

with the ordered magnetic moment aligned along the c axis at the ground state is thus suggested. A total of 135 reflections are collected at both 5.5 K and 1.6 K for the refinement of the magnetic structure. Given the magnetic propagation vector **k** = (0, 0, 0) and a strong c-axis Ising anisotropy, the Irrep Γ_3 with the basis vector $\psi_1 = (0, 0, 1)$ is used for magnetic structure refinement of TbV$_6$Sn$_6$. The ordered magnetic moment of Tb^{3+} is determined at 9.4(2) μ_B, which is very close to the effective moment of the free Tb^{3+}. The magnetic structure of TbV$_6$Sn$_6$ is shown in Fig. 6(e), in which the magnetic moment of Tb^{3+} is indeed aligned along the c axis, thus further confirming the strong easy c-axis anisotropy as suggested previously [63,64].

B. Magnetic Structure of DyV$_6$Sn$_6$

Figure 7 presents the single-crystal neutron diffraction results of DyV$_6$Sn$_6$. The temperature dependence of the (1, 0, 0) reflection clearly reveals a magnetic phase transition at 3.0 K [see Fig. 7(a)]. A total of 245 reflections are measured to determine the magnetic structure at both 5.0 K and 1.8 K. Among these reflections, as shown in Figs. 7(b)–7(e), a difference in intensity between 5.0 K and 1.8 K for the (0, 0, -6) reflection can be seen, suggesting that a projection of the ordered magnetic moment in the ab plane also exists. Similar intensity changes are also observed in the (-1, -1, -1), (-1, -1, 0), and (-1, 0, 0) reflections, which indicates the ordered
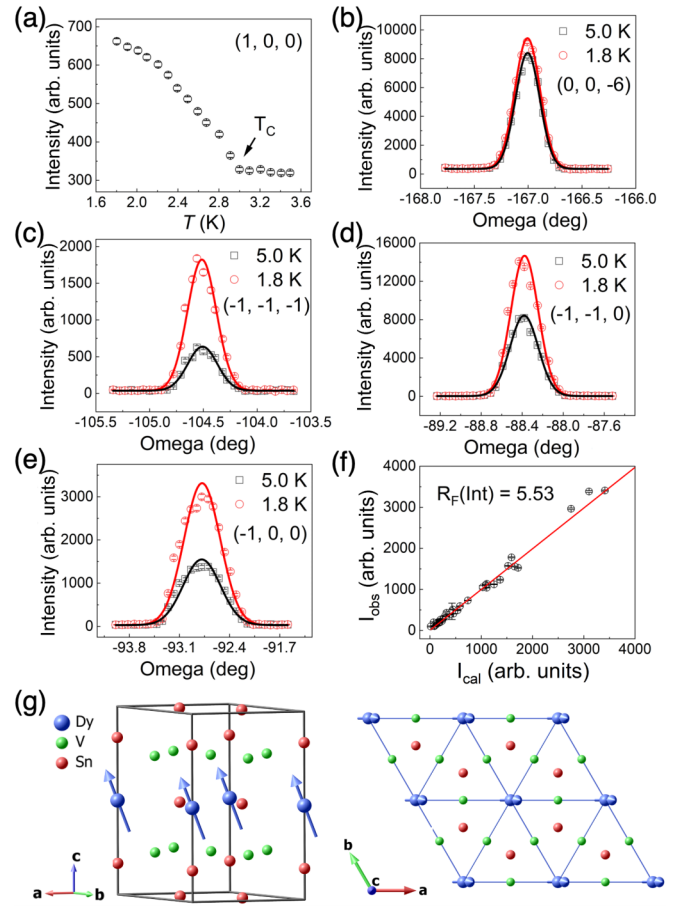

FIG. 7. Single-crystal neutron diffraction results of DyV$_6$Sn$_6$. (a) Temperature dependence from 1.8 K to 3.5 K of (1, 0, 0). (b)–(e) Omega scans at 5.0 K and 1.8 K of (0, 0, -6), (-1, -1, -1), (-1, -1, 0), and (-1, 0, 0), respectively. (g) Magnetic structure of DyV$_6$Sn$_6$ with the propagation vector **k** = (0, 0, 0) in custom and top view, and (f) fitted reflections as a function of observation and calculation.

magnetic moments of Dy^{3+} at 1.8 K is neither simply aligned along the c axis nor within the ab plane, but tilted away from them. A weak magnetic anisotropy is also suggested from the magnetization measurements of DyV$_6$Sn$_6$ [see Fig. 3(f)]. Given the magnetic propagation vector **k** = (0, 0, 0) and the identified weak magnetic anisotropy, both the Irreps Γ_3 and Γ_9 including the basis vectors $\psi_1 = (0, 0, 1)$, $\psi_2 = (1, 0, 0)$ and $\psi_3 = (1, 2, 0)$ are used in the refinement for DyV$_6$Sn$_6$, which is based on the measured 245 reflections after the neutron absorption correction. Furthermore, the magnetic structure refinement based on the symmetry-imposed and equally populated magnetic domains is also undertaken and the same result is obtained. The solved magnetic structure reveals a magnetic moment of Dy^{3+} as 6.6(2) μ_B ferromagnetically ordered inclined approximately 20° off from the c axis towards the [1, 0, 0] direction, as depicted in Fig. 7(g).

C. Magnetic Structure of HoV$_6$Sn$_6$

The single-crystal neutron diffraction results for HoV$_6$Sn$_6$ are displayed in Fig. 8. The (1, 1, 1) reflection is selected
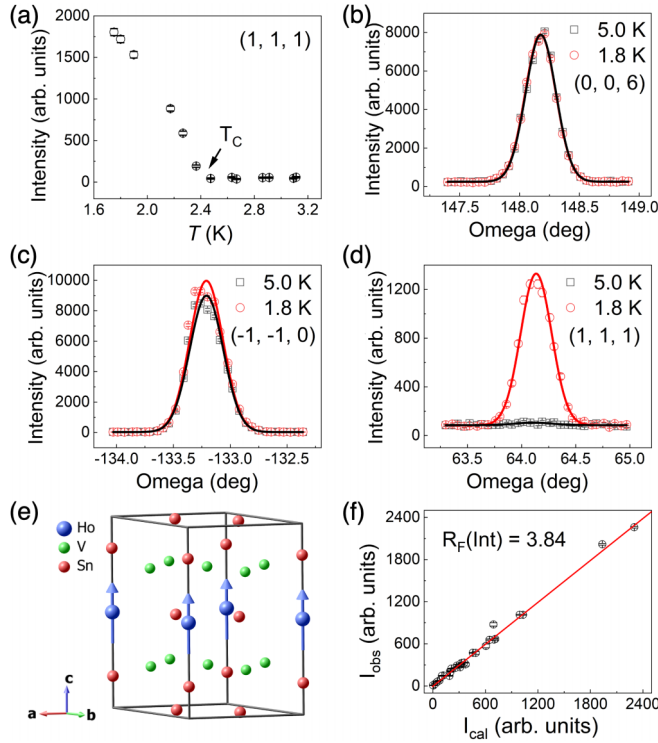
FIG. 8. Single-crystal neutron diffraction results of HoV_6Sn_6. (a) Temperature dependence from 1.8 K to 3.1 K of (1, 1, 1). (b)–(d) Omega scans at 5.0 K and 1.8 K of the (0, 0, 6), (-1, -1, 0), and (1, 1, 1) reflections, respectively. (e) Magnetic structure of HoV_6Sn_6 with the magnetic propagation vector $\mathbf{k} = (0, 0, 0)$, and (f) fitted reflections as a function of observation and calculation.

for the temperature dependence measurement. As shown in Fig. 8(a), the onset of the magnetic phase transition can be identified at 2.4 K. For the (0, 0, 6) reflection, similar to the case in TbV_6Sn_6, no noticeable intensity variation between 1.8 K and 5.0 K can be seen, thus suggesting that the ordered magnetic moment is aligned in parallel to the c axis. This finding is consistent with the magnetization results [see Fig. 3(g)]. Additionally, an increase in intensity is observed for the (-1, -1, 0) and (1, 1, 1) reflections at 1.8 K, which further supports that the magnetic moment of Ho^{3+} is aligned along the c axis. A total of 201 reflections were collected at both 5.0 K and 1.8 K. Based on the magnetic propagation vector $\mathbf{k} = (0, 0, 0)$ and a strong c-axis magnetic anisotropy, the Irrep Γ_3 with the basis vector $\psi_1 = (0, 0, 1)$ is adopted for the magnetic structure refinement of HoV_6Sn_6. The final analysis yields an ordered magnetic moment of Ho^{3+} as 6.4(2) μ_B, along the c axis. The magnetic structure is shown in Fig. 8(e).

D. Magnetic Structure of ErV$_6$Sn$_6$

The single-crystal neutron diffraction results for ErV_6Sn_6 are shown in Fig. 9. Magnetic reflections are found at the $(H, K, L \pm 0.5)$ positions. The temperature dependence measurement at (0, 0, 1.5) reveals that the magnetic transition happens at 0.6 K [see Fig. 9(a)]. Omega scans conducted at 0.1 K and 0.7 K on the (0, 0, 2.5) reflection are depicted
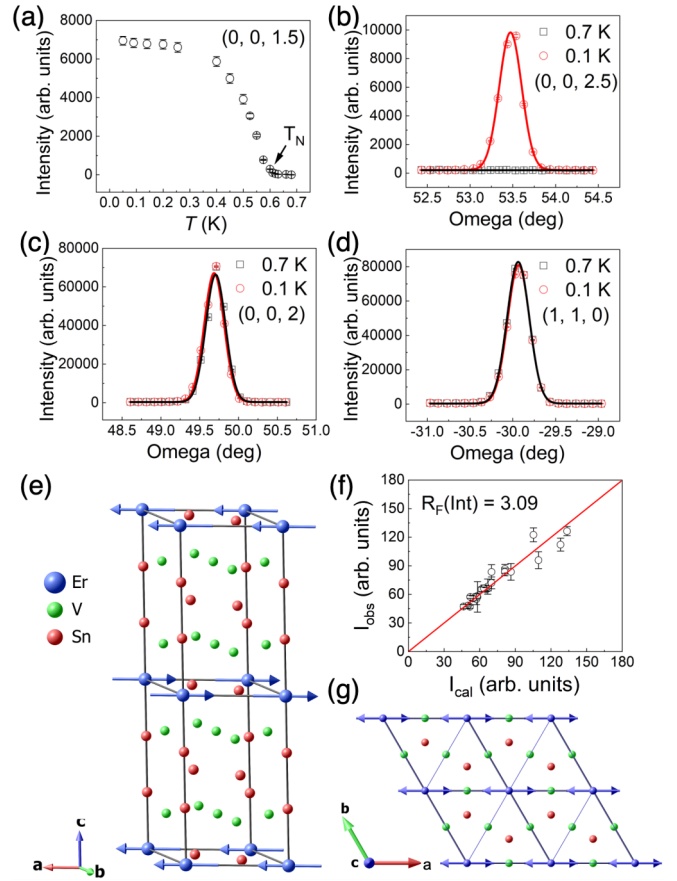

FIG. 9. Single-crystal neutron diffraction results of ErV_6Sn_6. (a) Temperature dependence from 0.05 K to 0.7 K of (0, 0, 1.5). (b)–(d) Omega scans at 0.1 K and 0.7 K of the (0, 0, 2.5), (0, 0, 2), and (1, 1, 0) reflections, respectively. Magnetic structure of ErV_6Sn_6 with the magnetic propagation vector $\mathbf{k} = (0, 0, 0.5)$ in (e) custom and (g) top view, and (f) fitted reflections as a function of observation and calculation.

in Fig. 9(b). At 0.1 K, a magnetic peak emerges at (0, 0, 2.5), indicating an antiferromagnetic structure with a magnetic propagation vector $\mathbf{k} = (0, 0, 0.5)$. The observed very weak intensity at the structural reflection (0, 0, 5) further rules out the possibility of second-order contamination originating from the structural reflections. Taking into account the significant magnetic anisotropy in the ab plane from its magnetization properties, it is suggested that the magnetic moment of Er^{3+} lies within the ab plane. In total, 211 structural and 148 magnetic reflections are measured to determine the magnetic structure at 50 mK. The neutron absorption correction is also undertaken for all the measured reflections via Mag2Pol. Based on the magnetic propagation vector $\mathbf{k} = (0, 0, 0.5)$ and the observed strong easy ab-plane magnetic anisotropy, the Irrep Γ_9 with the basis vectors $\psi_2 = (1, 0, 0)$ and $\psi_3 = (1, 2, 0)$ are used in the refinement for ErV_6Sn_6. The custom and top view of the solved magnetic structure is shown in Figs. 9(e) and 9(g). The final result reveals an ordered magnetic moment of Er^{3+} as 6.1(3) μ_B in its ground state, and an A-type antiferromagnetic order within the ab plane parallel to the a direction.
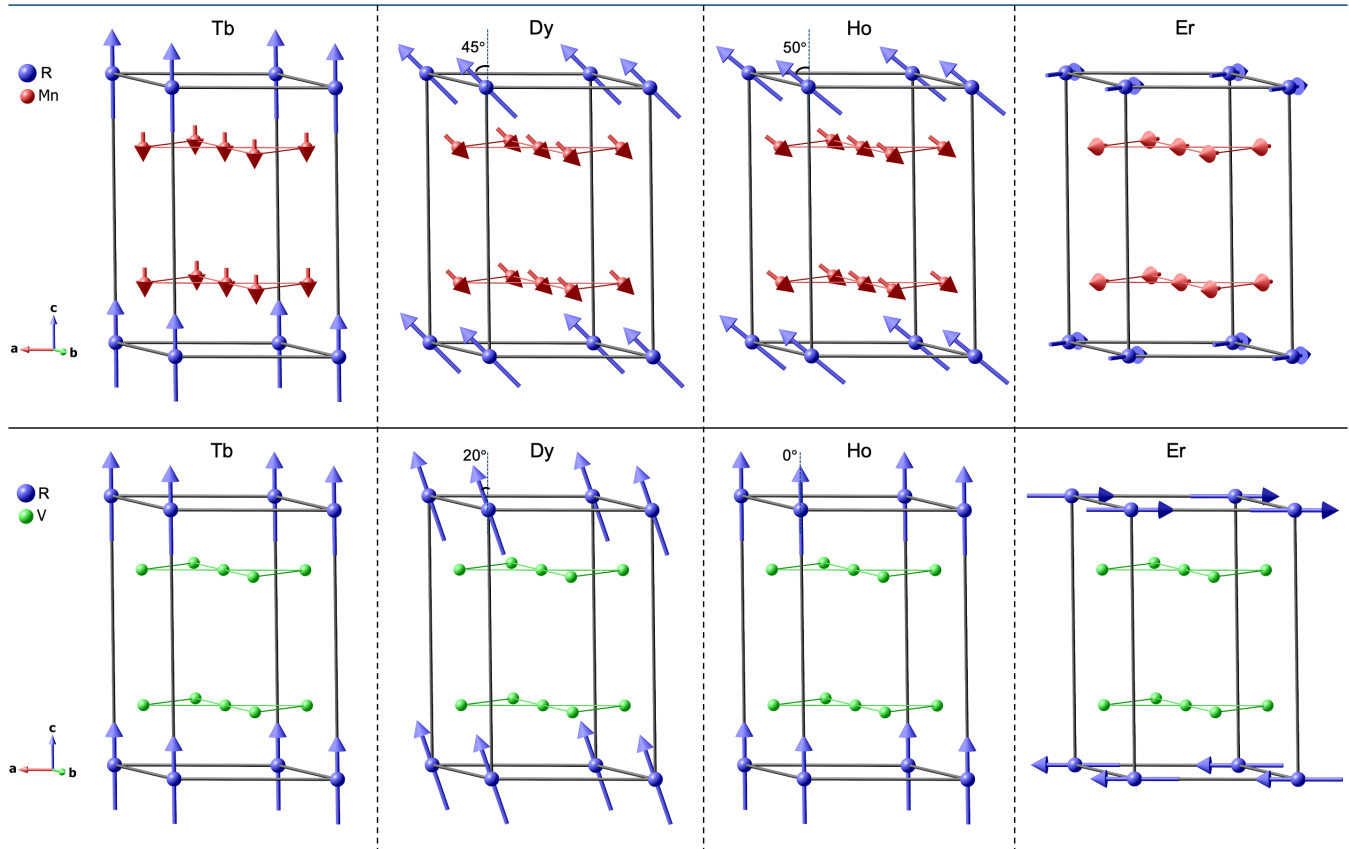
FIG. 10. Comparison of the ground-state magnetic structures of $R\text{Mn}_6\text{Sn}_6$ [25,45,46] and $R\text{V}_6\text{Sn}_6$ (R = Tb, Dy, Ho, Er).

V. DISCUSSIONS AND OUTLOOK

By investigating $R\text{V}_6\text{Sn}_6$, we not only uncover the intriguing physical properties of a new series of topological kagome metals, as discussed in the previous sections, but also could gain new insights into the complex magnetic orders and interactions in another extensively investigated magnetic kagome metal series of $R\text{Mn}_6\text{Sn}_6$. This is because $R\text{V}_6\text{Sn}_6$ represents a simplified case where Mn is replaced by nonmagnetic V, thus switching off the magnetism from Mn as well as the magnetic interactions between R and Mn. In this regard, YMn_6Sn_6 could serve as another simplified case for the understanding of the complex magnetism in $R\text{Mn}_6\text{Sn}_6$, as the magnetism from R and the corresponding R-Mn interactions are also removed.

Numerous neutron scattering studies on YMn_6Sn_6 [44,48,49,51] have revealed that under zero field it transforms initially to a commensurate AFM order with a propagation vector of (0, 0, 0.5) below 345 K, and, upon cooling to the base temperature, subsequently to a double-flat-spiral incommensurate magnetic order. This behavior is attributed to the strong intralayer Mn-Mn FM interaction due to a short distance ($\sim$2.8 Å) between the neighboring Mn ions, and the competing interlayer magnetic interactions owing to the slight difference in distances between the nonequivalent Mn layers (i.e., [Mn-Sn2-Sn1-Sn2-Mn] and [Mn-RSn3-Mn] layers) [44,76].

In $R\text{Mn}_6\text{Sn}_6$ (R = Tb, Dy, Ho, Er), magnetic orders vary significantly due to different R-Mn exchange interactions

[25,42,45–47,50,56,77]. For R = Tb, Dy, and Ho, the R and Mn moments exhibit FiM order below 423 K, 393 K, and 376 K, respectively, with a subsequent spin reorientation at 320 K (Tb), 277 K (Dy), and 195 K (Ho). In contrast, for ErMn_6Sn_6, an incommensurate magnetic spiral order appears below 345 K, which is then followed by an FiM order at 68 K. The high magnetic ordering temperatures in $R\text{Mn}_6\text{Sn}_6$ are due to the strong intralayer Mn-Mn and interlayer R-Mn interactions, while the spin reorientation transition is likely driven by the delicate balance between the magnetic anisotropy energy and the R-Mn interaction. Thus, the R-Mn interaction plays a crucial role in the $R\text{Mn}_6\text{Sn}_6$ system with the distance of $\sim$3.6 Å between the neighboring R and Mn ions.

In $R\text{V}_6\text{Sn}_6$, in which Mn is replaced by nonmagnetic V, the magnetic interactions become simpler, involving only intralayer and interlayer $R - R$ interactions. The indirect Ruderman-Kittel-Kasuya-Yosida (RKKY) exchange interaction dominates due to the relatively long distances between R ions (i.e., $\sim$5.5 Å for intralayer and $\sim$9.0 Å for interlayer $R - R$ interactions). In contrast to the strong Mn-Mn and R-Mn direct exchange interactions in $R\text{Mn}_6\text{Sn}_6$, the RKKY interaction is much weaker, so that the magnetic phase transition temperature is strongly suppressed in $R\text{V}_6\text{Sn}_6$. The ground-state magnetic structures of $R\text{Mn}_6\text{Sn}_6$ [25,45,46] and $R\text{V}_6\text{Sn}_6$ (R = Tb, Dy, Ho, Er) are summarized in Fig. 10. A comparison of them could help to unravel the crucial role of the $4f$-$3d$ R-Mn interactions played in the tuning of the magnetic properties of the $R\text{Mn}_6\text{Sn}_6$ system. The distinct

magnetic anisotropy of various R ions shows evidently in RV$_6$Sn$_6$: the ordered magnetic moment is aligned along the c axis for both TbV$_6$Sn$_6$ and HoV$_6$Sn$_6$, slightly tilted away from the c axis for DyV$_6$Sn$_6$, and aligned within the ab plane for ErV$_6$Sn$_6$, respectively. The ordering temperatures for RV$_6$Sn$_6$ are 4.3 K, 3.0 K, 2.4 K, and 0.6 K for the Tb, Dy, Ho, and Er compounds, respectively (see Table II). These temperatures follow the same trend as the spin-reorientation transition temperatures in RMn$_6$Sn$_6$ that decrease with increasing atomic number of the rare-earth elements, indicating a weaker R-Mn interaction for rare-earth elements with higher atomic numbers. This trend also suggests that the R-Mn interaction is significantly influenced by the intrinsic single-ion properties of R^{3+}, which strongly depend on crystalline electric field (CEF) effects. Additionally, the large difference in magnetic transition temperature between RV$_6$Sn$_6$ and RMn$_6$Sn$_6$ further indicates a robust R-Mn interaction.

There are numerous possible emergent quantum phenomena yet to be discovered in this system, particularly concerning the interplay between topology and magnetism. Unlike the RMn$_6$Sn$_6$ system, where the kagome layers are magnetic, the RV$_6$Sn$_6$ system features a nonmagnetic topological kagome layer and a magnetic triangular layer of R, thus providing a fresh platform for understanding such an interplay. For instance, when an out-of-plane magnetization is introduced to the kagome lattice in TbMn$_6$Sn$_6$, it lifts the spin degeneracy, thus transforming the Z_2 topological gap into a quantum-limit Chern gap, and resulting in the kagome lattice hosting exotic chiral edge states [1,23]. However, in the RMn$_6$Sn$_6$ system, the kagome layers are inherently magnetic, which breaks time-reversal symmetry and may significantly alter the electronic structure of the kagome lattice. This condition does not occur in the RV$_6$Sn$_6$ system, making it a perfect platform to study the interplay between magnetism and topology. The magnetic nature of R in the RV$_6$Sn$_6$ system can then be used as an ideal tuning parameter to explore how magnetism influences the topological features arising from the kagome geometry, offering insights that are unattainable in magnetic systems like RMn$_6$Sn$_6$. For instance, it would be very interesting to search for possible exotic quantum states like Chern insulator or Weyl semimetal at its ground state at very low temperatures in TbV$_6$Sn$_6$, owing to the ferromagnetically ordered large moment of Tb^{3+} along the c axis and the nonmagnetic V kagome layers. HoV$_6$Sn$_6$ may exhibit a similar but relatively weaker effect. Additionally, the spin Berry curvature [30], that is related to the bilayer kagome lattice, may also be systematically explored in the magnetically ordered states in RV$_6$Sn$_6$.

Another interesting aspect to discuss is the magnetic frustration in RV$_6$Sn$_6$ due to the presence of an ideal triangular lattice of the R site. However, the dominating FM intralayer $R - R$ interaction does not provide a strong basis for frustration, especially in the Ising-type ordered compound TbV$_6$Sn$_6$, with a magnetic moment of 9.4(2) μ_B ordered along the c axis. For DyV$_6$Sn$_6$ and HoV$_6$Sn$_6$, their magnetic moments at 1.8 K are still notably smaller than those of the free ions. In ErV$_6$Sn$_6$, the ordered magnetic moment is 6.1(3) μ_B at 50 mK, which is also much smaller than its free ion moment. This thus hints a likely strong influence of the single-ion CEF effects and possible presence of persistent spin fluctuations in the

ground state. Clearly, further studies of CEF excitations and spin dynamics would be of high interest.

VI. CONCLUSIONS

In this work, we report mainly a comprehensive single-crystal neutron diffraction investigation of the ground-state magnetic structures of the recently discovered V-based topological kagome metals RV$_6$Sn$_6$ (R = Tb, Dy, Ho, Er). We also systematically investigated the crystal structure, magnetic properties and specific heat capacity (down to 50 mK) of the high-quality single-crystal samples of this kagome metal series, that were successfully grown by the flux method, via a wide range of in-house characterization techniques. These in-house investigations indicate the presence of long-range magnetic order at low temperatures. Our single-crystal neutron diffraction measurements further confirm that the long-range magnetic order indeed takes place at 4.3 K (Tb), 3.0 K (Dy), 2.4 K (Ho), and 0.6 K (Er), respectively, and no further magnetic phase transitions were found at lower temperatures down to 50 mK according to the heat capacity results. The ground-state magnetic structures of all the studied compounds are comprehensively determined via the magnetic crystallography approaches. It can be revealed that RV$_6$Sn$_6$ (R = Tb, Dy, Ho) transform to a collinear ferromagnetic order below the magnetic phase transition temperature, with the ordered magnetic moment aligned along the c axis for R = Tb, Ho, while approximately 20° tilted off from the c axis for R = Dy. Due to an apparent antiferromagnetic interlayer coupling between triangular lattice Er layers, ErV$_6$Sn$_6$ shows an A-type antiferromagnetic structure with a magnetic propagation vector $\mathbf{k}$ = (0, 0, 0.5), and with the ordered moment aligned in the ab plane. The ordered magnetic moments are determined as 9.4(2) μ_B, 6.6(2) μ_B, 6.4(2) μ_B, and 6.1(2) μ_B for R = Tb, Dy, Ho, and Er, respectively. We also compared and discussed the low-temperature magnetic structures in both RV$_6$Sn$_6$ and RMn$_6$Sn$_6$ kagome metal series. This allows to gain new insights into the complex magnetic interactions, single-ion magnetic anisotropy and spin dynamics in these compounds. With the determined ground-state magnetic structures in these four compounds, further investigations on the possible interplay between magnetism and topologically nontrivial electron band structures in the magnetically ordered phase regime can be expected for this fascinating topological kagome metal series of RV$_6$Sn$_6$.

[1] J.-X. Yin, B. Lian, and M. Z. Hasan, Topological kagome magnets and superconductors, Nature (London) **612**, 647 (2022).

[2] N. J. Ghimire and I. I. Mazin, Topology and correlations on the kagome lattice, Nat. Mater. **19**, 137 (2020).

[3] X. Xu, J.-X. Yin, Z. Qu, and S. Jia, Quantum interactions in topological R166 kagome magnet, Rep. Prog. Phys. **86**, 114502 (2023).

[4] T. Neupert, M. M. Denner, J.-X. Yin, R. Thomale, and M. Z. Hasan, Charge order and superconductivity in kagome materials, Nat. Phys. **18**, 137 (2022).

[5] M. Kang, L. Ye, S. Fang, J.-S. You, A. Levitan, M. Han, J. I. Facio, C. Jozwiak, A. Bostwick, E. Rotenberg, M. K. Chan, R. D. McDonald, D. Graf, K. Kaznatcheev, E. Vescovo, D. C. Bell, E. Kaxiras, J. van den Brink, M. Richter, M. P. Ghimire *et al.*, Dirac fermions and flat bands in the ideal kagome metal FeSn, Nat. Mater. **19**, 163 (2020).

[6] Z. Liu, M. Li, Q. Wang, G. Wang, C. Wen, K. Jiang, X. Lu, S. Yan, Y. Huang, D. Shen, J.-X. Yin, Z. Wang, Z. Yin, H. Lei, and S. Wang, Orbital-selective Dirac fermions and extremely flat bands in frustrated kagome-lattice metal CoSn, Nat. Commun. **11**, 4002 (2020).

[7] M. Li, Q. Wang, G. Wang, Z. Yuan, W. Song, R. Lou, Z. Liu, Y. Huang, Z. Liu, H. Lei, Z. Yin, and S. Wang, Dirac cone, flat band and saddle point in kagome magnet YMn₆Sn₆, Nat. Commun. **12**, 3129 (2021).

[8] S. Nakatsuji, N. Kiyohara, and T. Higo, Large anomalous Hall effect in a non-collinear antiferromagnet at room temperature, Nature (London) **527**, 212 (2015).

[9] M. Ikhlas, T. Tomita, T. Koretsune, M.-T. Suzuki, D. Nishio-Hamane, R. Arita, Y. Otani, and S. Nakatsuji, Large anomalous Nernst effect at room temperature in a chiral antiferromagnet, Nat. Phys. **13**, 1085 (2017).

[10] M. Kimata, H. Chen, K. Kondou, S. Sugimoto, P. K. Muduli, M. Ikhlas, Y. Omori, T. Tomita, A. H. MacDonald, S. Nakatsuji, and Y. Otani, Magnetic and magnetic inverse spin Hall effects in a non-collinear antiferromagnet, Nature (London) **565**, 627 (2019).

[11] H. Tsai, T. Higo, K. Kondou, T. Nomoto, A. Sakai, A. Kobayashi, T. Nakano, K. Yakushiji, R. Arita, S. Miwa, Y. Otani, and S. Nakatsuji, Electrical manipulation of a topological antiferromagnetic state, Nature (London) **580**, 608 (2020).

[12] X. Li, J. Koo, Z. Zhu, K. Behnia, and B. Yan, Field-linear anomalous Hall effect and Berry curvature induced by spin chirality in the kagome antiferromagnet Mn₃Sn, Nat. Commun. **14**, 1642 (2023).

[13] Q. Wang, Y. Xu, R. Lou, Z. Liu, M. Li, Y. Huang, D. Shen, H. Weng, S. Wang, and H. Lei, Large intrinsic anomalous Hall effect in half-metallic ferromagnet Co₃Sn₂S₂ with magnetic Weyl fermions, Nat. Commun. **9**, 3681 (2018).

[14] D. F. Liu, A. J. Liang, E. K. Liu, Q. N. Xu, Y. W. Li, C. Chen, D. Pei, W. J. Shi, S. K. Mo, P. Dudin, T. Kim, C. Cacho, G. Li, Y. Sun, L. X. Yang, Z. K. Liu, S. S. P. Parkin, C. Felser, and Y. L. Chen, Magnetic Weyl semimetal phase in a kagome crystal, Science **365**, 1282 (2019).

[15] N. Morali, R. Batabyal, P. K. Nag, E. Liu, Q. Xu, Y. Sun, B. Yan, C. Felser, N. Avraham, and H. Beidenkopf, Fermi-arc diversity on surface terminations of the magnetic Weyl semimetal Co₃Sn₂S₂, Science **365**, 1286 (2019).

[16] Y. Xing, J. Shen, H. Chen, L. Huang, Y. Gao, Q. Zheng, Y.-Y. Zhang, G. Li, B. Hu, G. Qian, L. Cao, X. Zhang, P. Fan, R. Ma, Q. Wang, Q. Yin, H. Lei, W. Ji, S. Du, H. Yang *et al.*, Localized spin-orbit polaron in magnetic Weyl semimetal Co₃Sn₂S₂, Nat. Commun. **11**, 5613 (2020).

[17] S. Howard, L. Jiao, Z. Wang, N. Morali, R. Batabyal, P. Kumar-Nag, N. Avraham, H. Beidenkopf, P. Vir, E. Liu, C. Shekhar, C. Felser, T. Hughes, and V. Madhavan, Evidence for one-dimensional chiral edge states in a magnetic Weyl semimetal Co₃Sn₂S₂, Nat. Commun. **12**, 4269 (2021).

[18] T. Kida, L. A. Fenner, A. A. Dee, I. Terasaki, M. Hagiwara, and A. S. Wills, The giant anomalous Hall effect in the ferromagnet Fe₃Sn₂—a frustrated kagome metal, J. Phys.: Condens. Matter **23**, 112205 (2011).

[19] L. Ye, M. Kang, J. Liu, F. von Cube, C. R. Wicker, T. Suzuki, C. Jozwiak, A. Bostwick, E. Rotenberg, D. C. Bell, L. Fu, R. Comin, and J. G. Checkelsky, Massive Dirac fermions in a ferromagnetic kagome metal, Nature (London) **555**, 638 (2018).

[20] Z. Lin, J.-H. Choi, Q. Zhang, W. Qin, S. Yi, P. Wang, L. Li, Y. Wang, H. Zhang, Z. Sun, L. Wei, S. Zhang, T. Guo, Q. Lu, J.-H. Cho, C. Zeng, and Z. Zhang, Flatbands and emergent ferromagnetic ordering in Fe₃Sn₂ kagome lattices, Phys. Rev. Lett. **121**, 096401 (2018).

[21] J.-X. Yin, S. S. Zhang, H. Li, K. Jiang, G. Chang, B. Zhang, B. Lian, C. Xiang, I. Belopolski, H. Zheng, T. A. Cochran, S.-Y. Xu, G. Bian, K. Liu, T.-R. Chang, H. Lin, Z.-Y. Lu, Z. Wang, S. Jia, W. Wang, and M. Z. Hasan, Giant and anisotropic many-body spin–orbit tunability in a strongly correlated kagome magnet, Nature (London) **562**, 91 (2018).

[22] Y. Li, Q. Wang, L. DeBeer-Schmitt, Z. Guguchia, R. D. Desautels, J.-X. Yin, Q. Du, W. Ren, X. Zhao, Z. Zhang, I. A. Zaliznyak, C. Petrovic, W. Yin, M. Z. Hasan, H. Lei, and J. M. Tranquada, Magnetic-field control of topological electronic response near room temperature in correlated kagome magnets, Phys. Rev. Lett. **123**, 196604 (2019).

[23] J.-X. Yin, W. Ma, T. A. Cochran, X. Xu, S. S. Zhang, H.-J. Tien, N. Shumiya, G. Cheng, K. Jiang, B. Lian, Z. Song, G. Chang, I. Belopolski, D. Multer, M. Litskevich, Z.-J. Cheng, X. P. Yang, B. Swidler, H. Zhou, H. Lin *et al.*, Quantum-limit Chern topological magnetism in TbMn₆Sn₆, Nature (London) **583**, 533 (2020).

[24] X. Xu, J.-X. Yin, W. Ma, H.-J. Tien, X.-B. Qiang, P. V. S. Reddy, H. Zhou, J. Shen, H.-Z. Lu, T.-R. Chang, Z. Qu, and S. Jia, Topological charge-entropy scaling in kagome Chern magnet TbMn₆Sn₆, Nat. Commun. **13**, 1197 (2022).

[25] C. Mielke III, W. L. Ma, V. Pomjakushin, O. Zaharko, S. Sturniolo, X. Liu, V. Ukleev, J. S. White, J.-X. Yin, S. S. Tsirkin, C. B. Larsen, T. A. Cochran, M. Medarde, V. Porée, D. Das, R. Gupta, C. N. Wang, J. Chang, Z. Q. Wang, R. Khasanov *et al.*, Low-temperature magnetic crossover in the topological kagome magnet TbMn$_6$Sn$_6$, Commun. Phys. **5**, 107 (2022).

[26] S. X. M. Riberolles, T. J. Slade, R. L. Dally, P. M. Sarte, B. Li, T. Han, H. Lane, C. Stock, H. Bhandari, N. J. Ghimire, D. L. Abernathy, P. C. Canfield, J. W. Lynn, B. G. Ueland, and R. J. McQueeney, Orbital character of the spin-reorientation transition in TbMn$_6$Sn$_6$, Nat. Commun. **14**, 2658 (2023).

[27] X. Teng, J. S. Oh, H. Tan, L. Chen, J. Huang, B. Gao, J.-X. Yin, J.-H. Chu, M. Hashimoto, D. Lu, C. Jozwiak, A. Bostwick, E. Rotenberg, G. E. Granroth, B. Yan, R. J. Birgeneau, P. Dai, and M. Yi, Magnetism and charge density wave order in kagome FeGe, Nat. Phys. **19**, 814 (2023).

[28] H. W. S. Arachchige, W. R. Meier, M. Marshall, T. Matsuoka, R. Xue, M. A. McGuire, R. P. Hermann, H. Cao, and D. Mandrus, Charge density wave in kagome lattice intermetallic ScV$_6$Sn$_6$, Phys. Rev. Lett. **129**, 216402 (2022).

[29] T. Hu, H. Pi, S. Xu, L. Yue, Q. Wu, Q. Liu, S. Zhang, R. Li, X. Zhou, J. Yuan, D. Wu, T. Dong, H. Weng, and N. Wang, Optical spectroscopy and band structure calculations of the structural phase transition in the vanadium-based kagome metal ScV$_6$Sn$_6$, Phys. Rev. B **107**, 165119 (2023).

[30] D. Di Sante, C. Bigi, P. Eck, S. Enzner, A. Consiglio, G. Pokharel, P. Carrara, P. Orgiani, V. Polewczyk, J. Fujii, P. D. C. King, I. Vobornik, G. Rossi, I. Zeljkovic, S. D. Wilson, R. Thomale, G. Sangiovanni, G. Panaccione, and F. Mazzola, Flat band separation and robust spin Berry curvature in bilayer kagome metals, Nat. Phys. **19**, 1135 (2023).

[31] H. Tan and B. Yan, Abundant lattice instability in kagome metal ScV$_6$Sn$_6$, Phys. Rev. Lett. **130**, 266402 (2023).

[32] G. Pokharel, B. R. Ortiz, L. Kautzsch, S. J. G. Alvarado, K. Mallayya, G. Wu, E.-A. Kim, J. P. C. Ruff, S. Sarker, and S. D. Wilson, Frustrated charge order and cooperative distortions in ScV$_6$Sn$_6$, Phys. Rev. Mater. **7**, 104201 (2023).

[33] A. Korshunov, H. Hu, D. Subires, Y. Jiang, D. Călugăru, X. Feng, A. Rajapitamahuni, C. Yi, S. Roychowdhury, M. G. Vergniory, J. Strempfer, C. Shekhar, E. Vescovo, D. Chernyshov, A. H. Said, A. Bosak, C. Felser, B. A. Bernevig, and S. Blanco-Canosa, Softening of a flat phonon mode in the kagome ScV$_6$Sn$_6$, Nat. Commun. **14**, 6646 (2023).

[34] Z. Guguchia, D. J. Gawryluk, S. Shin, Z. Hao, C. Mielke Iii, D. Das, I. Plokhikh, L. Liborio, J. K. Shenton, Y. Hu, V. Sazgari, M. Medarde, H. Deng, Y. Cai, C. Chen, Y. Jiang, A. Amato, M. Shi, M. Z. Hasan, J.-X. Yin *et al.*, Hidden magnetism uncovered in a charge ordered bilayer kagome material ScV$_6$Sn$_6$, Nat. Commun. **14**, 7796 (2023).

[35] A. Subedi, Order-by-disorder charge density wave condensation at q = (1/3, 1/3, 1/3) in kagome metal ScV$_6$Sn$_6$, Phys. Rev. Mater. **8**, 014006 (2024).

[36] Y. Hu, J. Ma, Y. Li, Y. Jiang, D. J. Gawryluk, T. Hu, J. Teyssier, V. Multian, Z. Yin, S. Xu, S. Shin, I. Plokhikh, X. Han, N. C. Plumb, Y. Liu, J.-X. Yin, Z. Guguchia, Y. Zhao, A. P. Schnyder, X. Wu *et al.*, Phonon promoted charge density wave in topological kagome metal ScV$_6$Sn$_6$, Nat. Commun. **15**, 1658 (2024).

[37] Y.-X. Jiang, J.-X. Yin, M. M. Denner, N. Shumiya, B. R. Ortiz, G. Xu, Z. Guguchia, J. He, M. S. Hossain, X. Liu, J. Ruff, L. Kautzsch, S. S. Zhang, G. Chang, I. Belopolski, Q. Zhang, T. A. Cochran, D. Multer, M. Litskevich, Z.-J. Cheng *et al.*, Unconventional chiral charge order in kagome superconductor KV$_3$Sb$_5$, Nat. Mater. **20**, 1353 (2021).

[38] H. Chen, H. Yang, B. Hu, Z. Zhao, J. Yuan, Y. Xing, G. Qian, Z. Huang, G. Li, Y. Ye, S. Ma, S. Ni, H. Zhang, Q. Yin, C. Gong, Z. Tu, H. Lei, H. Tan, S. Zhou, C. Shen *et al.*, Roton pair density wave in a strong-coupling kagome superconductor, Nature (London) **599**, 222 (2021).

[39] S.-Y. Yang, Y. Wang, B. R. Ortiz, D. Liu, J. Gayles, E. Derunova, R. Gonzalez-Hernandez, L. Šmejkal, Y. Chen, S. S. P. Parkin, S. D. Wilson, E. S. Toberer, T. McQueen, and M. N. Ali, Giant, unconventional anomalous Hall effect in the metallic frustrated magnet candidate, KV$_3$Sb$_5$, Sci. Adv. **6**, eabb6003 (2020).

[40] B. R. Ortiz, L. C. Gomes, J. R. Morey, M. Winiarski, M. Bordelon, J. S. Mangum, I. W. H. Oswald, J. A. Rodriguez-Rivera, J. R. Neilson, S. D. Wilson, E. Ertekin, T. M. McQueen, and E. S. Toberer, New kagome prototype materials: Discovery of KV$_3$Sb$_5$, RbV$_3$Sb$_5$ and CsV$_3$Sb$_5$, Phys. Rev. Mater. **3**, 094407 (2019).

[41] H. Zhao, H. Li, B. R. Ortiz, S. M. L. Teicher, T. Park, M. Ye, Z. Wang, L. Balents, S. D. Wilson, and I. Zeljkovic, Cascade of correlated electron states in the kagome superconductor CsV$_3$Sb$_5$, Nature (London) **599**, 216 (2021).

[42] G. Venturini, B. C. E. Idrissi, and B. Malaman, Magnetic properties of RMn$_6$Sn$_6$ (R = Sc, Y, Gd-Tm, Lu) compounds with HfFe$_6$Ge$_6$ type structure, J. Magn. Magn. Mater. **94**, 35 (1991).

[43] G. Venturini, R. Welter, B. Malaman, and E. Ressouche, Magnetic structure of YMn$_6$Ge$_6$ and room temperature magnetic structure of LuMn$_6$Sn$_6$ obtained from neutron diffraction study, J. Alloys Compd. **200**, 51 (1993).

[44] G. Venturini, D. Fruchart, and B. Malaman, Incommensurate magnetic structures of RMn$_6$Sn$_6$ (R = Sc, Y, Lu) compounds from neutron diffraction study, J. Alloys Compd. **236**, 102 (1996).

[45] B. Malaman, G. Venturini, R. Welter, J. P. Sanchez, P. Vulliet, and E. Ressouche, Magnetic properties of RMn$_6$Sn$_6$ (R = Gd-Er) compounds from neutron diffraction and Mössbauer measurements, J. Magn. Magn. Mater. **202**, 519 (1999).

[46] B. C. El Idrissi, G. Venturini, B. Malaman, and D. Fruchart, Magnetic structures of TbMn$_6$Sn$_6$ and HoMn$_6$Sn$_6$ compounds from neutron diffraction study, J. Less-Common Met. **175**, 143 (1991).

[47] S. Kimura, A. Matsuo, S. Yoshii, K. Kindo, L. Zhang, E. Brück, K. H. J. Buschow, F. R. de Boer, C. Lefèvre, and G. Venturini, High-field magnetization of RMn$_6$Sn$_6$ compounds with R = Gd, Tb, Dy and Ho, J. Alloys Compd. **408-412**, 169 (2006).

[48] N. J. Ghimire, R. L. Dally, L. Poudel, D. C. Jones, D. Michel, N. T. Magar, M. Bleuel, M. A. McGuire, J. S. Jiang, J. F. Mitchell, J. W. Lynn, and I. I. Mazin, Competing magnetic phases and fluctuation-driven scalar spin chirality in the kagome metal YMn$_6$Sn$_6$, Sci. Adv. **6**, eabe2680 (2020).

[49] R. L. Dally, J. W. Lynn, N. J. Ghimire, D. Michel, P. Siegfried, and I. I. Mazin, Chiral properties of the zero-field spiral state

and field-induced magnetic phases of the itinerant kagome metal YMn_6Sn_6, Phys. Rev. B **103**, 094413 (2021).

[50] G. Dhakal, F. C. Kabeer, A. K. Pathak, F. Kabir, N. Poudel, R. Filippone, J. Casey, A. P. Sakhya, S. Regmi, C. Sims, K. Dimitri, P. Manfrinetti, K. Gofryk, P. M. Oppeneer, and M. Neupane, Anisotropically large anomalous and topological Hall effect in a kagome magnet, Phys. Rev. B **104**, L161115 (2021).

[51] Q. Wang, K. J. Neubauer, C. Duan, Q. Yin, S. Fujitsu, H. Hosono, F. Ye, R. Zhang, S. Chi, K. Krycka, H. Lei, and P. Dai, Field-induced topological Hall effect and double-fan spin structure with a c-axis component in the metallic kagome antiferromagnetic compound YMn_6Sn_6, Phys. Rev. B **103**, 014416 (2021).

[52] W. Ma, X. Xu, Z. Wang, H. Zhou, M. Marshall, Z. Qu, W. Xie, and S. Jia, Anomalous Hall effect in the distorted kagome magnets (Nd, Sm)Mn_6Sn_6, Phys. Rev. B **103**, 235109 (2021).

[53] W. Ma, X. Xu, J.-X. Yin, H. Yang, H. Zhou, Z.-J. Cheng, Y. Huang, Z. Qu, F. Wang, M. Z. Hasan, and S. Jia, Rare earth engineering in RMn_6Sn_6 (R = Gd-Tm, Lu) topological kagome magnets, Phys. Rev. Lett. **126**, 246602 (2021).

[54] L. Gao, S. Shen, Q. Wang, W. Shi, Y. Zhao, C. Li, W. Cao, C. Pei, J.-Y. Ge, G. Li, J. Li, Y. Chen, S. Yan, and Y. Qi, Anomalous Hall effect in ferrimagnetic metal RMn_6Sn_6 (R = Tb, Dy, Ho) with clean Mn kagome lattice, Appl. Phys. Lett. **119**, 092405 (2021).

[55] H. Zhang, J. Koo, C. Xu, M. Sretenovic, B. Yan, and X. Ke, Exchange-biased topological transverse thermoelectric effects in a kagome ferrimagnet, Nat. Commun. **13**, 1091 (2022).

[56] S. X. M. Riberolles, T. Han, T. J. Slade, J. M. Wilde, A. Sapkota, W. Tian, Q. Zhang, D. L. Abernathy, L. D. Sanjeewa, S. L. Bud'ko, P. C. Canfield, R. J. McQueeney, and B. G. Ueland, New insight into tuning magnetic phases of RMn_6Sn_6 kagome metals, npj Quantum Mater. **9**, 42 (2024).

[57] G. Pokharel, S. M. L. Teicher, B. R. Ortiz, P. M. Sarte, G. Wu, S. Peng, J. He, R. Seshadri, and S. D. Wilson, Electronic properties of the topological kagome metals YV_6Sn_6 and GdV_6Sn_6, Phys. Rev. B **104**, 235139 (2021).

[58] J. Lee and E. Mun, Anisotropic magnetic property of single crystals RV_6Sn_6 (R = Y, Gd - Tm, Lu), Phys. Rev. Mater. **6**, 083401 (2022).

[59] X. Zhang, Z. Liu, Q. Cui, Q. Guo, N. Wang, L. Shi, H. Zhang, W. Wang, X. Dong, J. Sun, Z. Dun, and J. Cheng, Electronic and magnetic properties of intermetallic kagome magnets RV_6Sn_6 (R = Tb-Tm), Phys. Rev. Mater. **6**, 105001 (2022).

[60] S. Peng, Y. Han, G. Pokharel, J. Shen, Z. Li, M. Hashimoto, D. Lu, B. R. Ortiz, Y. Luo, H. Li, M. Guo, B. Wang, S. Cui, Z. Sun, Z. Qiao, S. D. Wilson, and J. He, Realizing kagome band structure in two-dimensional kagome surface state of RV_6Sn_6 (R = Gd, Ho), Phys. Rev. Lett. **127**, 266401 (2021).

[61] Y. Hu, X. Wu, Y. Yang, S. Gao, N. C. Plumb, A. P. Schnyder, W. Xie, J. Ma, and M. Shi, Tunable topological Dirac surface states and van Hove singularities in kagome metal GdV_6Sn_6, Sci. Adv. **8**, eadd2024 (2022).

[62] Z. Porter, G. Pokharel, J.-W. Kim, P. J. Ryan, and S. D. Wilson, Incommensurate magnetic order in the $\mathbb{Z}_2$ kagome metal GdV_6Sn_6, Phys. Rev. B **108**, 035134 (2023).

[63] E. Rosenberg, J. M. DeStefano, Y. Guo, J. S. Oh, M. Hashimoto, D. Lu, R. J. Birgeneau, Y. Lee, L. Ke, M. Yi, and J.-H. Chu, Uniaxial ferromagnetism in the kagome metal TbV_6Sn_6, Phys. Rev. B **106**, 115139 (2022).

[64] G. Pokharel, B. Ortiz, J. Chamorro, P. Sarte, L. Kautzsch, G. Wu, J. Ruff, and S. D. Wilson, Highly anisotropic magnetism in the vanadium-based kagome metal TbV_6Sn_6, Phys. Rev. Mater. **6**, 104202 (2022).

[65] X. Huang, Z. Cui, C. Huang, M. Huo, H. Liu, J. Li, F. Liang, L. Chen, H. Sun, B. Shen, Y. Zhang, and M. Wang, Anisotropic magnetism and electronic properties of the kagome metal SmV_6Sn_6, Phys. Rev. Mater. **7**, 054403 (2023).

[66] K. Guo, J. Ye, S. Guan, and S. Jia, Triangular Kondo lattice in YbV_6Sn_6 and its quantum critical behavior in a magnetic field, Phys. Rev. B **107**, 205151 (2023).

[67] X.-Y. Zeng, H. Wang, X.-Y. Wang, J.-F. Lin, J. Gong, X.-P. Ma, K. Han, Y.-T. Wang, Z.-Y. Dai, and T.-L. Xia, Magnetic and magnetotransport properties in the vanadium-based kagome metals DyV_6Sn_6 and HoV_6Sn_6, Phys. Rev. B **109**, 104412 (2024).

[68] V. Petříček, M. Dušek, and L. Palatinus, Crystallographic Computing system JANA2006: General features, Z. Kristallogr. Krist. **229**, 345 (2014).

[69] N. Qureshi, *Mag*2*Pol*: A program for the analysis of spherical neutron polarimetry, flipping ratio and integrated intensity data, J. Appl. Crystallogr. **52**, 175 (2019).

[70] S. T. Bramwell, M. J. Harris, B. C. den Hertog, M. J. P. Gingras, J. S. Gardner, D. F. McMorrow, A. R. Wildes, A. L. Cornelius, J. D. M. Champion, R. G. Melko, and T. Fennell, Spin correlations in $Ho_2Ti_2O_7$: A dipolar spin ice system, Phys. Rev. Lett. **87**, 047205 (2001).

[71] C. M. N. Kumar, Y. Xiao, H. S. Nair, J. Voigt, B. Schmitz, T. Chatterji, N. H. Jalarvo, and T. Brückel, Hyperfine and crystal field interactions in multiferroic $HoCrO_3$, J. Phys.: Condens. Matter **28**, 476001 (2016).

[72] I. Mirebeau, A. Apetrei, J. Rodríguez-Carvajal, P. Bonville, A. Forget, D. Colson, V. Glazkov, J. P. Sanchez, O. Isnard, and E. Suard, Ordered spin ice state and magnetic fluctuations in $Tb_2Sn_2O_7$, Phys. Rev. Lett. **94**, 246402 (2005).

[73] J. Kim, X. Wang, F.-T. Huang, Y. Wang, X. Fang, X. Luo, Y. Li, M. Wu, S. Mori, D. Kwok, E. D. Mun, V. S. Zapf, and S.-W. Cheong, Spin liquid state and topological structural defects in hexagonal $TbInO_3$, Phys. Rev. X **9**, 031005 (2019).

[74] A. Wills, A new protocol for the determination of magnetic structures using simulated annealing and representational analysis (SARA*h*), Phys. B: Condens. Matter **276-278**, 680 (2000).

[75] F. Zhu, X. Wang, M. Meven, J. Song, T. Mueller, C. Yi, W. Ji, Y. Shi, J. Ma, K. Schmalzl, W. F. Schmidt, Y. Su, and T. Brückel, Magnetic structures, spin-flop transition, and coupling of Eu and Mn magnetism in the Dirac semimetal $EuMnBi_2$, Phys. Rev. Res. **2**, 043100 (2020).

[76] E. V. Rosenfeld and N. V. Mushnikov, Double-flat-spiral magnetic structures: Theory and application to the RMn_6X_6 compounds, Phys. B **403**, 1898 (2008).

[77] Z. Wang, J. Xu, Z. Li, T. Xu, J. Li, T. Zhao, J. Cai, Y. Zhang, and B. Shen, Real-space observation of magnetic transitions in RMn_6Sn_6 (R = Ho, Dy) kagome magnets, Appl. Phys. Lett. **122**, 112401 (2023).